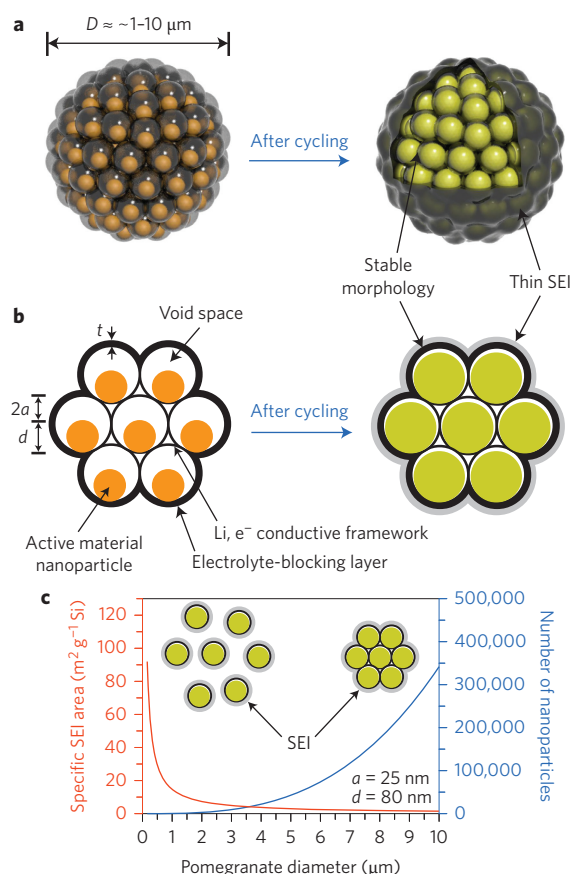


# A pomegranate-inspired nanoscale design for large-volume-change lithium battery anodes

Nian Liu<sup>1†</sup>, Zhenda Lu<sup>2†</sup>, Jie Zhao<sup>2</sup>, Matthew T. McDowell<sup>2</sup>, Hyun-Wook Lee<sup>2</sup>, Wenting Zhao<sup>2</sup> and Yi Cui<sup>2,3\*</sup>

Silicon is an attractive material for anodes in energy storage devices<sup>1–3</sup>, because it has ten times the theoretical capacity of its state-of-the-art carbonaceous counterpart. Silicon anodes can be used both in traditional lithium-ion batteries and in more recent Li–O<sub>2</sub> and Li–S batteries as a replacement for the dendrite-forming lithium metal anodes. The main challenges associated with silicon anodes are structural degradation and instability of the solid-electrolyte interphase caused by the large volume change (~300%) during cycling, the occurrence of side reactions with the electrolyte, and the low volumetric capacity when the material size is reduced to a nanometre scale<sup>4–7</sup>. Here, we propose a hierarchical structured silicon anode that tackles all three of these problems. Our design is inspired by the structure of a pomegranate, where single silicon nanoparticles are encapsulated by a conductive carbon layer that leaves enough room for expansion and contraction following lithiation and delithiation. An ensemble of these hybrid nanoparticles is then encapsulated by a thicker carbon layer in micrometre-size pouches to act as an electrolyte barrier. As a result of this hierarchical arrangement, the solid-electrolyte interphase remains stable and spatially confined, resulting in superior cyclability (97% capacity retention after 1,000 cycles). In addition, the microstructures lower the electrode–electrolyte contact area, resulting in high Coulombic efficiency (99.87%) and volumetric capacity (1,270 mAh cm<sup>–3</sup>), and the cycling remains stable even when the areal capacity is increased to the level of commercial lithium-ion batteries (3.7 mAh cm<sup>–2</sup>).

Particle fracture and loss of electrical contact have long been identified as primary reasons for the capacity fading of silicon-based anodes. Pioneering works have shown that decreasing the feature size to the nanoscale allows for the material to withstand the large (de)lithiation strains without fracture<sup>8–16</sup>. However, the cycle life of nanosized silicon is still limited due to the unstable solid-electrolyte interphase (SEI) on the surface. At the working potential of anodes (<0.5 V versus Li/Li<sup>+</sup>), the organic electrolyte decomposes and forms a thin SEI layer<sup>17–19</sup>. When the silicon expands and contracts, the SEI layer deforms and breaks. The formation of new SEI on the freshly exposed silicon surface causes the cell to have poor Coulombic efficiency, with the accumulated SEI eventually blocking Li<sup>+</sup> transport. As a consequence of this mechanism, even if most of the silicon active material remains electrically connected, the capacity decays as the SEI thickens. To control SEI formation, an electrolyte blocking layer and an internal void space need to be engineered into the structure. Such a design has been demonstrated in a few examples, including double-walled silicon nanotube and Si–C yolk–shell structures<sup>20–25</sup>, yielding



**Figure 1 | Schematic of the pomegranate-inspired design.** **a, b**, Three-dimensional view (**a**) and simplified two-dimensional cross-section view (**b**) of one pomegranate microparticle before and after electrochemical cycling (in the lithiated state). The nanoscale size of the active-material primary particles prevents fracture on (de)lithiation, whereas the micrometre size of the secondary particles increases the tap density and decreases the surface area in contact with the electrolyte. The self-supporting conductive carbon framework blocks the electrolyte and prevents SEI formation inside the secondary particle, while facilitating lithium transport throughout the whole particle. The well-defined void space around each primary particle allows it to expand without deforming the overall morphology, so the SEI outside the secondary particle is not ruptured during cycling and remains thin. **c**, Calculated surface area in contact with electrolyte (specific SEI area) and the number of primary nanoparticles in one pomegranate particle versus its diameter.

<sup>1</sup>Department of Chemistry, Stanford University, Stanford, California 94305, USA, <sup>2</sup>Department of Materials Science and Engineering, Stanford University, Stanford, California 94305, USA, <sup>3</sup>Stanford Institute for Materials and Energy Sciences, SLAC National Accelerator Laboratory, 2575 Sand Hill Road, Menlo Park, California 94025, USA, <sup>†</sup>These authors contributed equally to this work. \*e-mail: yicui@stanford.edu

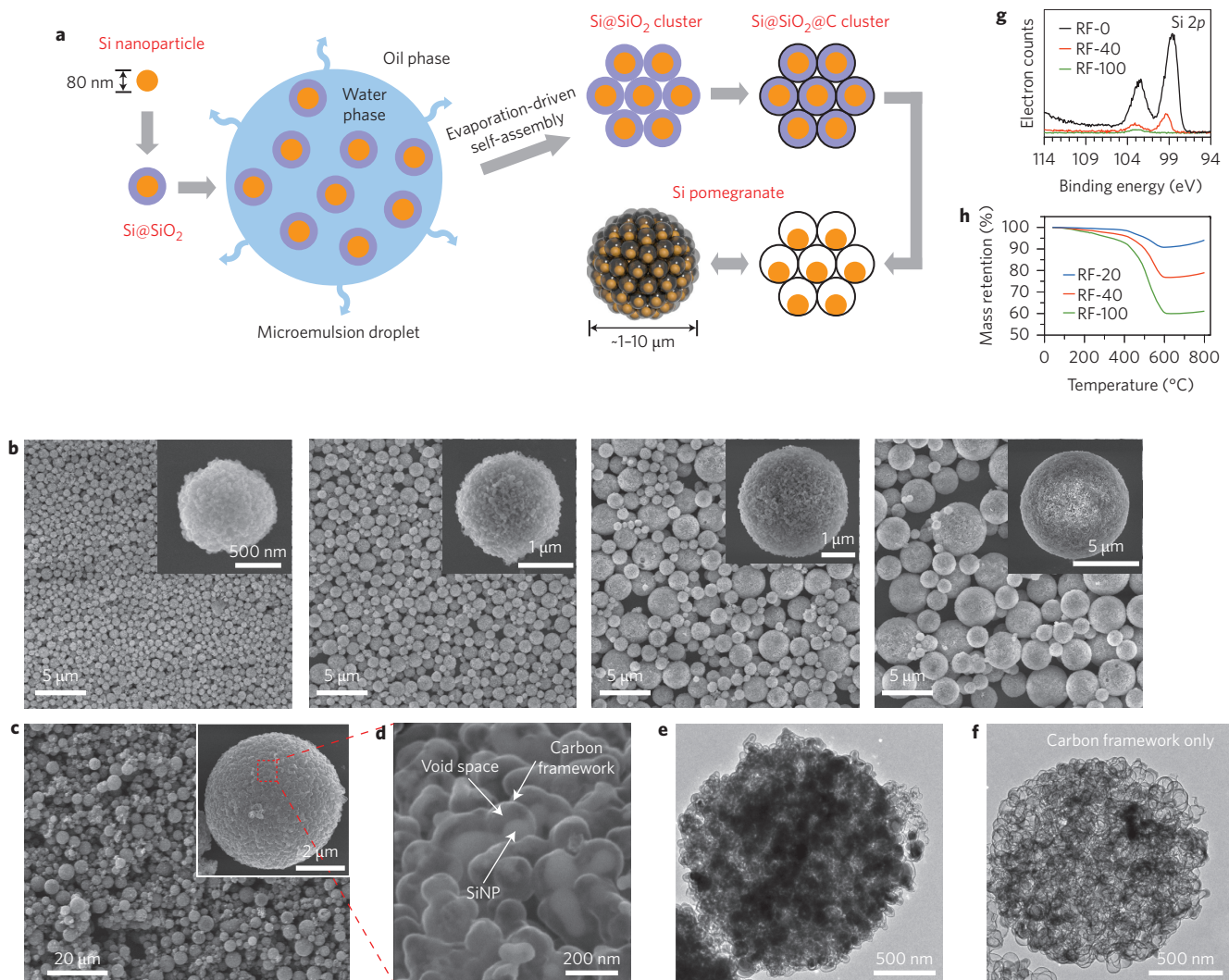


**Figure 2 | Fabrication and characterization of silicon pomegranates.** **a**, Schematic of the fabrication process for silicon pomegranates. **b**, SEM images of a series of silicon nanoparticle clusters with different diameters assembled by the microemulsion approach. The insets show magnified images of the individual microparticles. **c**, SEM images of silicon pomegranates showing the micrometre-sized and spherical morphology. **d**, Magnified SEM image showing the local structure of silicon nanoparticles and the conductive carbon framework with well-defined void space between. **e**, TEM image of one silicon pomegranate particle. **f**, TEM image of the carbon framework after etching away silicon using NaOH. **g,h**, High-resolution XPS spectra of Si 2p peaks (**g**) and thermogravimetric profiles (**h**) of silicon pomegranates with different thicknesses of carbon framework. X in 'RF-X' denotes X mg of resorcinol used for each 100 mg of Si@SiO<sub>2</sub> in the RF coating step (see Supplementary Methods). RF-0 denotes silicon nanoparticle clusters without carbon.

significant improvement in cycle life with relatively low areal mass loading ( $<0.2 \text{ mg cm}^{-2}$ ).

Although nanostructuring has been successful in extending the cycle life of silicon, nanostructured electrodes have introduced new fundamental challenges, including higher surface area, low tap density and generally poor electrical properties due to the higher interparticle resistance. The high surface area increases side reactions with the electrolyte and lowers the Coulombic efficiency. The low tap density leads to low volumetric capacity and a thick electrode at high mass loading, which makes it difficult to maintain electrical and ionic pathways during cycling. Finally, electrical contact between the nanoparticles is easily altered or diminished by volume changes during cycling, severely decreasing the cycle life of the electrode. To the best of our knowledge, stable cycling (100 cycles) with an areal capacity higher than  $3 \text{ mAh cm}^{-2}$  has not been reported.

Here, inspired by the structure of a pomegranate fruit, we demonstrate a novel secondary structure for silicon anodes (Fig. 1a,b). Such a design has multiple advantages: (1) the nanosized

primary particle size prevents fracture; (2) the well-defined internal void space allows the silicon to expand without changing the secondary particle size; (3) the carbon framework functions as an electrical highway and a mechanical backbone so that all nanoparticles are electrochemically active; (4) carbon completely encapsulates the entire secondary particle, limiting most SEI formation to the outer surface instead of on individual nanoparticles, which not only limits the amount of SEI, but also retains the internal void space for silicon expansion; and (5) the dilemma of high surface area and low tap density introduced when using nanosized primary features is partially solved. With this design, the specific SEI area (the surface area in contact with the electrolyte divided by the mass of silicon) decreases from  $\sim 90 \text{ m}^2 \text{ g}^{-1}$  for single yolk-shell particles to  $\sim 15 \text{ m}^2 \text{ g}^{-1}$  for  $1 \mu\text{m}$  secondary particles and to only  $1.5 \text{ m}^2 \text{ g}^{-1}$  for  $10 \mu\text{m}$  particles (Fig. 1c). At the same time, because of the space-efficient packing inside the secondary particles, their tap density is significantly higher than primary nanosized particles packed randomly. In the simplified demonstration shown in Supplementary Fig. 1, silicon nanoparticles have a tap density of

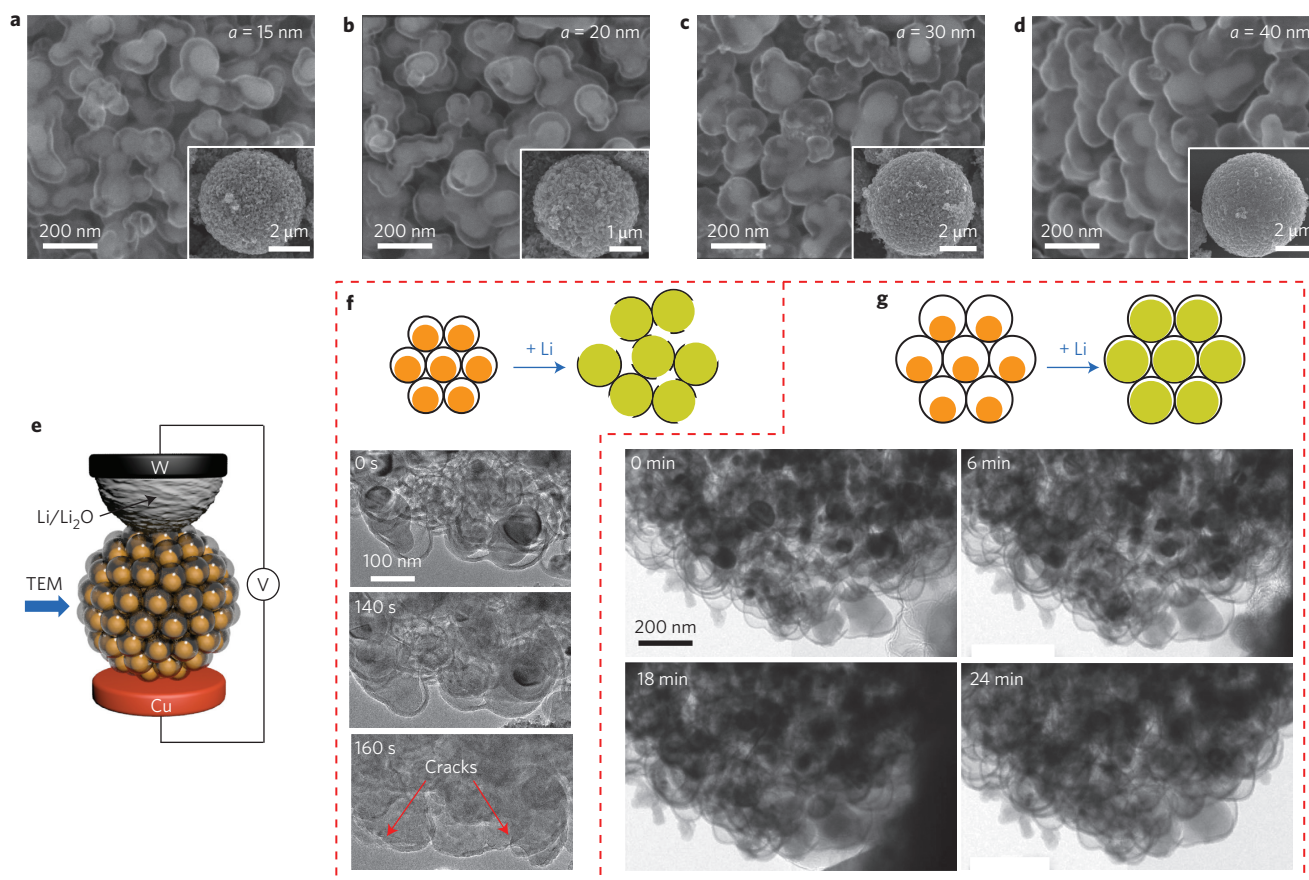


**Figure 3 | Tuning the size of the void space of silicon pomegranates and *in situ* TEM characterization during lithiation.** **a–d**, SEM images of as-synthesized silicon pomegranates with a void space size of 15 nm (**a**), 20 nm (**b**), 30 nm (**c**) and 40 nm (**d**), respectively. The definition of void space size is shown in Fig. 1b. **e**, Schematic of the *in situ* TEM device. **f**, Schematic and time-lapse images of the lithiation of silicon pomegranates with insufficient ( $\sim 15$  nm) void space (Supplementary Movie 1). Lithium transports along and across the carbon framework to react with the silicon inside, causing volume expansion. Because the void space is insufficient, the carbon framework is ruptured by the expansion of the silicon, and the overall morphology is destroyed. **g**, Lithiation of a silicon pomegranate with sufficient ( $\sim 40$  nm) void space (Supplementary Movie 2); the nanoparticles expand within the carbon framework and the carbon framework does not rupture. The secondary particle morphology is therefore intact on lithiation.

$0.15 \text{ g cm}^{-2}$ , while micrometre-sized clusters have a tap density of  $0.53 \text{ g cm}^{-2}$ , which represents an increase of 250%. This tap density is within the desirable range for electrodes because the volume expansion of silicon is up to 300%.

We have developed a bottom-up microemulsion<sup>26</sup> approach to synthesize highly spherical silicon pomegranate microbeads ranging from 500 nm to 10  $\mu\text{m}$  in diameter (Fig. 2a,b, Supplementary Figs 2–5). Silicon nanoparticles are individually encapsulated by the carbon framework, with well-defined void spaces between the silicon and carbon (Fig. 2c–e) that accommodate the volume expansion of the silicon. The carbon framework, although only a few nanometres thick, firmly supports the whole microbead (Fig. 2f, Supplementary Figs 6 and 7). X-ray photoelectron spectroscopy (XPS) results indicate complete coverage of carbon (Fig. 2g), which is crucial for blocking the electrolyte and limiting the majority of SEI formation to the outer surface of the microbeads. Our unique pomegranate design is fundamentally different from previous reports of silicon/carbon composite secondary particles<sup>11,27,28</sup>. First, the carbon component functions not only as a conducting framework, but also as an electrolyte-blocking layer, so SEI forms mostly outside the secondary particle. Second, the void spaces inside the secondary particle are well-defined and evenly distributed around each nanoparticle, and effectively accommodate the volume expansion of the silicon without rupturing the carbon shell or changing the secondary particle size. The initial well-defined void spaces do not decrease

the volumetric capacity, because they are designed to be mostly occupied in the lithiated state.

A sufficient and well-defined internal void space is necessary to maintain the structural integrity of the silicon anode. To identify the critical gap size, we synthesized silicon pomegranates with a series of gap sizes by tuning the thickness of the  $\text{SiO}_2$  sacrificial layer (Fig. 3a–d). We then performed an *in situ* transmission electron microscopy (TEM) study of their structural change on lithiation. The *in situ* TEM set-up is based on previous studies<sup>29,30</sup> and is shown schematically in Fig. 3e. For a silicon pomegranate with insufficient ( $\sim 15$  nm) gap size, as shown in Fig. 3f and Supplementary Movie 1, the expanded Li–Si first occupies all the void spaces and then ruptures the carbon shell and causes structural degradation. This kind of crack formation in a conventional battery configuration will cause (1) excessive formation of SEI, (2) loss of electrical connection to the active material and (3) whole-electrode-level cracking due to accumulated particle shuffling across the thickness of the electrode. In the case of sufficient gap size (Fig. 3g and Supplementary Movie 2), however, silicon expands inside the carbon framework to occupy the void spaces, resulting in little change to both the carbon shell and secondary particle size. Taking into account the initial size of the nanoparticles ( $\sim 80$  nm) and their size distribution, silicon pomegranates with a  $\sim 30$ – $40$  nm gap size are the most promising, so this gap size was chosen for further electrochemical characterization. The fact that the nanoparticles in the middle of the secondary particle are

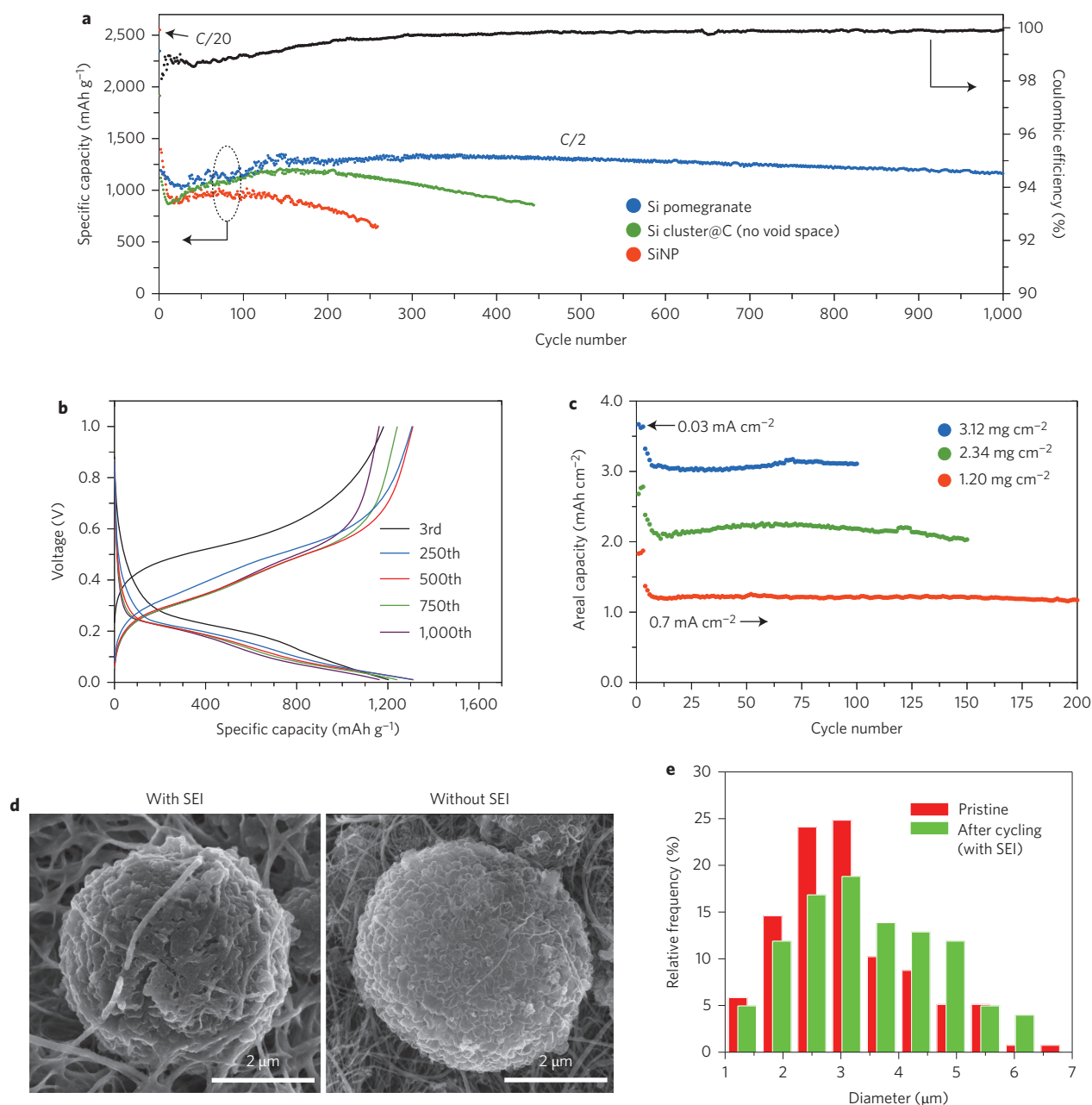


**Figure 4 | Electrochemical characterization of silicon pomegranate anodes.** All specific capacities of silicon pomegranate anodes are based on the total mass of the active materials (silicon and carbon in the pomegranate structure). **a**, Reversible delithiation capacity for the first 1,000 galvanostatic cycles of the silicon pomegranate and other structures tested under the same conditions. Coulombic efficiency is plotted for the silicon pomegranate only. The mass loading of the active material was  $\sim 0.2 \text{ mg cm}^{-2}$ . The rate was C/20 for the first cycle and C/2 for later cycles. ( $1\text{C} = 4.2 \text{ A g}^{-1}$  active material). **b**, Voltage profiles for the silicon pomegranate plotted for the 3rd, 250th, 500th, 750th and 1,000th cycles. **c**, High areal mass loading test (up to  $3.12 \text{ mg cm}^{-2}$  active material) of silicon pomegranate anodes. All electrodes were first cycled at  $0.03 \text{ mA cm}^{-2}$  for three cycles and  $0.7 \text{ mA cm}^{-2}$  for later cycles. **d**, Typical SEM images of silicon pomegranates after 100 cycles. **e**, Statistical analysis of silicon pomegranate diameter before and after 100 cycles, with averages of 3.1 and 3.4  $\mu\text{m}$ , respectively.

active upon lithiation suggests effective lithium transport along and across the carbon shell and framework.

The pomegranate design affords remarkable battery performance. As shown in Fig. 4a, its reversible capacity reached  $2,350 \text{ mAh g}^{-1}$  at a rate of C/20 ( $1\text{C} = \text{charge/discharge in 1 h}$ ). If not mentioned, all reported capacities are based on the total mass of silicon and carbon in the pomegranate structure. Because silicon is only 77% of the mass of the pomegranate structure, the capacity with respect to silicon is as high as  $3,050 \text{ mAh g}^{-1}$ . The volumetric capacity based on electrode volume was determined

to be  $1,270 \text{ mAh cm}^{-3}$ , which is more than twice the  $600 \text{ mAh cm}^{-3}$  obtained for graphite anodes<sup>6</sup>. From the 2nd to 1,000th cycle at a rate of C/2, the capacity retention was more than 97%. After 1,000 cycles, over  $1,160 \text{ mAh g}^{-1}$  capacity remained, which is more than three times the theoretical capacity of graphite. The cycle stability (0.003% decay per cycle) is among the best cycling performances of silicon anodes reported to date. Furthermore, it was achieved with a conventional polyvinylidene fluoride (PVDF) binder, which has been considered a poor binder for silicon anodes<sup>13</sup>. Under the same conditions, secondary particles

without an internal void space (nanoparticle clusters directly coated by carbon) demonstrated significant decay after 200 cycles. Bare nanoparticles decayed even more quickly. The voltage profiles of silicon pomegranate electrodes (Fig. 4b) exhibited typical electrochemical features of silicon, with little change over 1,000 cycles. Coulombic efficiency is an indicator of the reversibility of the electrode reaction. SEI rupture and reformation usually results in decreased Coulombic efficiency, especially in later cycles. The average Coulombic efficiency from the 500th to 1,000th cycles of the silicon pomegranate is as high as 99.87% (Fig. 4a, Supplementary Fig. 8). At a relatively slow rate of  $C/2$ , this Coulombic efficiency is superior to most previous reports.

It should be noted that many publications only report specific capacity normalized by the weight of the active materials, and low areal mass loading is frequently used to achieve stable cycling. However, high areal mass loading is needed to realize high performance based on total cell weight or volume<sup>31</sup>. We therefore tested thick silicon pomegranate electrodes with active material mass loading up to  $3.12 \text{ mg cm}^{-2}$  (silicon and carbon in a pomegranate structure). Following deep cycling at  $0.03 \text{ mA cm}^{-2}$ , the reversible areal capacity reached  $3.67 \text{ mAh cm}^{-2}$  (Fig. 4c), similar to, if not higher than, the capacity in a commercial lithium-ion battery cell. From the 4th to 100th cycle at a higher rate of  $0.7 \text{ mA cm}^{-2}$ , the capacity retention was as high as 94%. After 100 deep cycles, the areal capacity was still above  $3 \text{ mAh cm}^{-2}$ . To the best of our knowledge, high capacity and stable cycling at such a mass loading level have rarely been reported for silicon anodes. At slightly lower mass loadings of 2.34 and  $1.20 \text{ mg cm}^{-2}$ , 150 and 200 stable cycles were achieved. The specific capacity of the high mass loading cell ( $950 \text{ mAh g}^{-1}$ ) is only slightly lower than that of the low mass loading cell shown in Fig. 4a, which indicates that almost all the silicon pomegranate is active in the thick electrode. Further high loading cells also demonstrated stable cycling (Supplementary Fig. 9). Stable cycling of a high mass loading cell has strict requirements in terms of structural stability at the particle level, because even small changes in particle morphology could accumulate across the thickness of the electrode and cause electrode-level cracking and failure. Excellent performance at high mass loading indicates successful design of the pomegranate structure.

There are two interdependent characteristics of the pomegranate design that enable superior battery performance. The first is the internally accommodated volume expansion, which retains the structural integrity of the secondary particles and stabilizes the SEI on the surface. After 100 deep cycles, the morphology of the silicon pomegranates was examined with scanning electron microscopy (SEM; Fig. 4d). Nearly perfect spherical micrometre-sized particles were observed, with thin and uniform SEI coating the surface. After removing the SEI with acid, intact carbon shells with silicon inside are clearly visible. Statistical analysis of the diameter of the silicon pomegranates before and after cycling (Fig. 4e) shows only a 10% increase from  $3.1 \mu\text{m}$  to  $3.4 \mu\text{m}$  due to the formation of an SEI layer. The volume change here is much less than that of bare alloying anode, and is as small as intercalation-type graphite particles<sup>6</sup>, which is crucial for excellent performance in volume change-sensitive, high mass loading cells.

The second characteristic is spatially confined SEI formation. Our pomegranate particles are fundamentally different from previously reported secondary particles that have open inner surfaces<sup>11,27,28</sup>, in that they have an electrolyte-blocking layer that limits most of the SEI formation to the surface of the secondary particle (Supplementary Figs 10 and 11). Also, the internally accommodated volume expansion ensures that the SEI on the secondary particle is thin and stable. This mechanism not only decreases the quantity of SEI, but also enables the inner void space to be retained,

even after many cycles. As shown in Fig. 4e, the thickness of the outer SEI layer is only  $\sim 150 \text{ nm}$ , similar to that of double-walled silicon nanotubes<sup>20</sup>. In addition, because the SEI is on a micrometre-sized secondary particle, the relative quantity of SEI is significantly reduced compared to that on primary nanostructures (Fig. 1c). The thin, stable and spatially confined SEI increases the Coulombic efficiency and improves cycle stability.

An additional advantage of silicon pomegranates is that they exist in the form of powders, and their synthesis does not involve any complex equipment or processes such as chemical vapour deposition. Hence, they are entirely compatible with conventional slurry-coating manufacturing for lithium-ion battery electrodes. However, we note that future work is needed to reduce the cost of starting materials such as the silicon nanoparticles to meet commercial needs. The initial Coulombic efficiency is 82% for 9% carbon, but decreases with increasing thickness of the carbon coating (75% Coulombic efficiency at 23% carbon) (Fig. 2h, Supplementary Fig. 12), and is still lower than state-of-the-art graphite anodes due to the high density of lithium trapping sites in amorphous carbon (Supplementary Fig. 13). It still needs to be improved further, possibly by performing prelithiation<sup>32</sup> or replacing amorphous carbon with another material that does not irreversibly trap large amounts of lithium.

## Methods

**Synthesis.** As illustrated in Fig. 2a, commercial silicon nanoparticles were first coated with a  $\text{SiO}_2$  layer using tetraethoxysilane<sup>21</sup>. The aqueous dispersion of  $\text{Si@SiO}_2$  nanoparticles was then mixed with 1-octadecene containing 0.3 wt% emulsifier<sup>26</sup> to form water-in-oil emulsions. After evaporation of water at  $\sim 95\text{--}98^\circ\text{C}$ , the assembled  $\text{Si@SiO}_2$  nanoparticle clusters were collected by centrifugation, followed by heat treatment at  $550^\circ\text{C}$  for 1 h in air to remove the organics and condense the cluster structures. A low-cost, step-growth polymerization in the presence of ammonia then generated a resorcinol-formaldehyde resin (RF) layer to wrap the cluster, which was converted into a carbon layer under argon at  $800^\circ\text{C}$ . The thickness of the carbon layer could be tuned by changing the added amount of resorcinol monomer<sup>33</sup>. Finally, the  $\text{SiO}_2$  sacrificial layer was removed with 5 wt% HF solution to form a void space to accommodate the large volume change of silicon material during the charge/discharge process. For more details, see Supplementary Materials and Methods.

**In situ TEM.** A specialized dual-probe electrical biasing holder (Nanofactory Instruments) was used. By biasing the working electrode between  $-2.5$  and  $-3 \text{ V}$  versus the counter electrode,  $\text{Li}^+$  ions flow through the oxide/nitride layer and are reduced at the working electrode, where they react with carbon and alloy with the silicon in the pomegranate structure. The lithiation time of a silicon pomegranate structure is less than 30 min (Fig. 3g), corresponding to  $2C$ . The small size of the primary nanoparticles and the conductive carbon framework synergistically lead to good kinetics, as also evidenced by the rate performance of half cells shown in Supplementary Fig. 14.

**Electrochemistry.** The battery performance was evaluated by galvanostatic cycling of coin cells with the silicon pomegranate structures as the working electrode and lithium foil as the counter/reference electrode. The working electrodes were made using a typical slurry method with silicon pomegranate powders, carbon black and PVDF binder with a mass ratio of 8:1:1; the mass loading of active material (silicon and carbon in the pomegranate structure) was  $\sim 0.2 \text{ mg cm}^{-2}$ . All the cells were cycled between 0.01 and 1 V versus  $\text{Li/Li}^+$ . To prepare high mass loading electrodes, as shown in Fig. 4c, silicon pomegranate microbeads and carbon nanotubes (mass ratio 7:3) were dispersed in *N*-methyl-2-pyrrolidone (NMP) and filtered to make a binder-free microbead/carbon nanotube paper, which was cut into discs, with mass loading from 1 to  $3 \text{ mg cm}^{-2}$ . The electrolyte was 1.0 M  $\text{LiPF}_6$  in 1:1 wt/wt ethylene carbonate/diethyl carbonate, with 1 vol% vinylene carbonate added to improve the cycling stability. This type of filtered electrode has a density of  $\sim 0.4 \text{ g cm}^{-3}$ . The thickness is  $\sim 120 \mu\text{m}$  when the silicon pomegranate loading is  $3.12 \text{ mg cm}^{-2}$ . The volumetric capacity based on electrode volume is  $310 \text{ mAh cm}^{-3}$ . This value is lower than graphite, but it should be noted that such filtered electrodes are not calendared and 30% carbon nanotubes increases the volume of the electrode. They are intentionally not calendared to show the excellent and robust intraparticle conductivity of the silicon pomegranates without the need for pressure. To examine whether the silicon pomegranate could perform well in denser electrodes, we also tested high-loading electrodes fabricated using an industry-viable slurry coating and calendaring process with much fewer carbon nanotubes (5%) or no nanotubes. These electrodes also demonstrated stable cycling at high areal capacity (Supplementary Fig. 9), as well as much higher volumetric capacity ( $\sim 900\text{--}1,270 \text{ mAh cm}^{-3}$ ) than the practical value for graphite anodes ( $< 600 \text{ mAh cm}^{-3}$ ).

Received 19 August 2013; accepted 10 January 2014;  
published online 16 February 2014

## References

- Armand, M. & Tarascon, J.-M. Building better batteries. *Nature* **451**, 652–657 (2008).
- Arico, A. S., Bruce, P., Scrosati, B., Tarascon, J.-M. & van Schalkwijk, W. Nanostructured materials for advanced energy conversion and storage devices. *Nature Mater.* **4**, 366–377 (2005).
- Bruce, P. G., Freunberger, S. A., Hardwick, L. J. & Tarascon, J.-M. Li–O<sub>2</sub> and Li–S batteries with high energy storage. *Nature Mater.* **11**, 19–29 (2012).
- Beaulieu, L. Y., Eberman, K. W., Turner, R. L., Krause, L. J. & Dahn, J. R. Colossal reversible volume changes in lithium alloys. *Electrochem. Solid-State Lett.* **4**, A137–A140 (2001).
- Obrovac, M. N. & Christensen, L. Structural changes in silicon anodes during lithium insertion/extraction. *Electrochem. Solid-State Lett.* **7**, A93–A96 (2004).
- Obrovac, M. N., Christensen, L., Le, D. B. & Dahn, J. R. Alloy design for lithium-ion battery anodes. *J. Electrochem. Soc.* **154**, A849–A855 (2007).
- Larcher, D. *et al.* Recent findings and prospects in the field of pure metals as negative electrodes for Li-ion batteries. *J. Mater. Chem.* **17**, 3759–3772 (2007).
- Chan, C. K. *et al.* High-performance lithium battery anodes using silicon nanowires. *Nature Nanotech.* **3**, 31–35 (2008).
- Wu, H. & Cui, Y. Designing nanostructured Si anodes for high energy lithium ion batteries. *Nano Today* **7**, 414–429 (2012).
- Park, M.-H. *et al.* Silicon nanotube battery anodes. *Nano Lett.* **9**, 3844–3847 (2009).
- Magasinski, A. *et al.* High-performance lithium-ion anodes using a hierarchical bottom-up approach. *Nature Mater.* **9**, 353–358 (2010).
- Deshpande, R., Cheng, Y.-T. & Verbrugge, M. W. Modeling diffusion-induced stress in nanowire electrode structures. *J. Power Sources* **195**, 5081–5088 (2010).
- Liu, G. *et al.* Polymers with tailored electronic structure for high capacity lithium battery electrodes. *Adv. Mater.* **23**, 4679–4683 (2011).
- Lee, S. W., McDowell, M. T., Berla, L. A., Nix, W. D. & Cui, Y. Fracture of crystalline silicon nanopillars during electrochemical lithium insertion. *Proc. Natl Acad. Sci. USA* **109**, 4080–4085 (2012).
- Hwang, T. H., Lee, Y. M., Kong, B.-S., Seo, J.-S. & Choi, J. W. Electrospun core-shell fibers for robust silicon nanoparticle-based lithium ion battery anodes. *Nano Lett.* **12**, 802–807 (2012).
- Yi, R., Dai, F., Gordin, M. L., Chen, S. & Wang, D. Micro-sized Si–C composite with interconnected nanoscale building blocks as high-performance anodes for practical application in lithium-ion batteries. *Adv. Energy Mater.* **3**, 295–300 (2013).
- Aurbach, D. Review of selected electrode–solution interactions which determine the performance of Li and Li ion batteries. *J. Power Sources* **89**, 206–218 (2000).
- Chan, C. K., Ruffo, R., Hong, S. S. & Cui, Y. Surface chemistry and morphology of the solid electrolyte interphase on silicon nanowire lithium-ion battery anodes. *J. Power Sources* **189**, 1132–1140 (2009).
- Verma, P., Maire, P. & Novák, P. A review of the features and analyses of the solid electrolyte interphase in Li-ion batteries. *Electrochim. Acta* **55**, 6332–6341 (2010).
- Wu, H. *et al.* Stable cycling of double-walled silicon nanotube battery anodes through solid-electrolyte interphase control. *Nature Nanotech.* **7**, 310–315 (2012).
- Liu, N. *et al.* A yolk-shell design for stabilized and scalable Li-ion battery alloy anodes. *Nano Lett.* **12**, 3315–3321 (2012).
- Li, X. *et al.* Hollow core–shell structured porous Si–C nanocomposites for Li-ion battery anodes. *J. Mater. Chem.* **22**, 11014–11017 (2012).
- Chen, S. *et al.* Silicon core–hollow carbon shell nanocomposites with tunable buffer voids for high capacity anodes of lithium-ion batteries. *Phys. Chem. Chem. Phys.* **14**, 12741–12745 (2012).
- Park, Y. *et al.* Si-encapsulating hollow carbon electrodes via electroless etching for lithium-ion batteries. *Adv. Energy Mater.* **3**, 206–212 (2012).
- Wang, B. *et al.* Contact-engineered and void-involved silicon/carbon nanohybrids as lithium-ion-battery anodes. *Adv. Mater.* **25**, 3560–3565 (2013).
- Cho, Y.-S., Yi, G.-R., Kim, S.-H., Pine, D. J. & Yang, S.-M. Colloidal clusters of microspheres from water-in-oil emulsions. *Chem. Mater.* **17**, 5006–5013 (2005).
- Yin, Y.-X., Xin, S., Wan, L.-J., Li, C.-J. & Guo, Y.-G. Electro spray synthesis of silicon/carbon nanoporous microspheres as improved anode materials for lithium-ion batteries. *J. Phys. Chem. C* **115**, 14148–14154 (2011).
- Jung, D. S., Hwang, T. H., Park, S. B. & Choi, J. W. Spray drying method for large-scale and high-performance silicon negative electrodes in Li-ion batteries. *Nano Lett.* **13**, 2092–2097 (2013).
- Huang, J. Y. *et al.* *In situ* observation of the electrochemical lithiation of a single SnO<sub>2</sub> nanowire electrode. *Science* **330**, 1515–1520 (2010).
- McDowell, M. T. *et al.* *In situ* TEM of two-phase lithiation of amorphous silicon nanospheres. *Nano Lett.* **13**, 758–764 (2013).
- De Volder, M. F. L., Tawfick, S. H., Baughman, R. H. & Hart, A. J. Carbon nanotubes: present and future commercial applications. *Science* **339**, 535–539 (2013).
- Liu, N., Hu, L., McDowell, M. T., Jackson, A. & Cui, Y. Prelithiated silicon nanowires as an anode for lithium ion batteries. *ACS Nano* **5**, 6487–6493 (2011).
- Li, N. *et al.* Sol-gel coating of inorganic nanostructures with resorcinol-formaldehyde resin. *Chem. Commun.* **49**, 5135–5137 (2013).

## Acknowledgements

Y.C. acknowledges support from the Assistant Secretary for Energy Efficiency and Renewable Energy, Office of Vehicle Technologies of the US Department of Energy (contract no. DE-AC02-05CH11231, subcontract no. 6951379) under the Batteries for Advanced Transportation Technologies (BATT) Program. M.T.M. acknowledges the National Science Foundation Graduate Fellowship Program and the Stanford Graduate Fellowship Program. H.W.L. acknowledges the Basic Science Research Program through the National Research Foundation of Korea (NRF) funded by the Ministry of Education, Science and Technology (contract no. 2012038593). The authors thank Z. Chen for discussions, F. Wei for providing the carbon nanotubes and Croda for providing the emulsifier.

## Author contributions

N.L., Z.L. and Y.C. conceived the concept and experiments. N.L. and Z.L. carried out the synthesis and performed materials characterization and electrochemical measurements. J.Z. participated in part of the synthesis and electrochemical measurements. M.T.M. and H.W.L. conducted *in situ* TEM characterization. W.Z. conducted focused ion beam experiments. N.L., Z.L. and Y.C. co-wrote the paper. All authors discussed the results and commented on the manuscript.

## Additional information

Supplementary information is available in the [online version](#) of the paper. Reprints and permissions information is available online at [www.nature.com/reprints](http://www.nature.com/reprints). Correspondence and requests for materials should be addressed to Y.C.

## Competing financial interests

The authors declare no competing financial interests.